Journal of The Electrochemical Society, **150** (2) F20-F27 (2003)
0013-4651/2003/150(2)/F20/8/$7.00 © The Electrochemical Society, Inc.

Low Temperature Radio-Frequency-Sputtered (Ba, Sr)TiO_3 Films on Pt/TiN/Ti/Si Substrates with Various Oxygen/Argon Mixing Ratios

Der-Chi Shye,[a] Bi-Shiou Chiou,[a,z] Ming-Jiunn Lai,[a] Chuan-Chou Hwang,[a] Cheng-Chung Jiang,[b] Jyh-Shin Chen,[b] Ming-Hwu Cheng,[b] and Huang-Chung Cheng[b,*]

[a]*Department of Electronics Engineering and Institute of Electronics, National Chiao Tung University, Hsinchu 30010, Taiwan*
[b]*Precision Instrument Development Center, National Science Council, Hsingchu Science-Based Industrial Park, Hsinchu 300, Taiwan*

(Ba,Sr)TiO_3 (BST) films were fabricated on Pt/TiN/Ti/Si substrates by low temperature radio frequency magnetron cosputtering at 300°C. Material and electrical properties of BST films sputtered at low temperatures are significantly affected by the $O_2/(Ar + O_2)$ mixing ratio (OMR). Plasma emission spectra indicate that the deposition rate declines at a higher OMR due to oxide formation on the target surface. The dielectric constant of the BST films can reach a maximum of 364 at 5% OMR. The ten-year lifetime of the time-dependent dielectric breakdown implies that the reliability of the capacitor can be enhanced at a higher OMR due to compensation of oxygen vacancies and smaller grain sizes. Current-voltage analysis indicates that the leakage current of the Pt/BST/Pt capacitor is limited by Schottky emission (SE)/Poole-Frenkel emission (PF) at a lower/higher applied field. The applied field boundary between SE and PF shifts toward higher field as OMR increases. Moreover, an energy band model was proposed and this leakage mechanism was discussed.
 [DOI: 10.1149/1.1536179].

Manuscript submitted January 23, 2002; revised manuscript received June 21, 2002. Available electronically January 9, 2003.

(Ba, Sr)TiO_3 (BST) films have been investigated as capacitors for giga-bit dynamic random access memory (DRAM) applications because of their high dielectric constants (ε_r). The capacitor over bit line (COB) is adopted to structure the high density DRAMs and thus shrink the cell. High temperature (>450°C) deposition of BST films is frequently applied to obtain good crystallinity of a perovskite structure,[1,2] but the high temperature process may deform the junction profile and alter the gate length of the metal-oxide-semiconductor field-emission-transistor (MOSFET), especially on the deep submicrometer scale.

Besides, the metal/TiN/Ti/polysilicon-plug structure is generally proposed as a bottom electrode of a standard COB-DRAM-capacitor.[3,4] The Pt/TiN/Ti/Si substrates exhibit better adhesion and interfacial stress than do Pt/SiO_2/Si substrates, but the interdiffusion and chemical reaction of TiN/Ti layers should be carefully controlled. The Ti layer forms $TiSi_x$ to improve the adhesion and the contact properties between TiN and polysilicon, and the TiN barrier layer prevents diffusion of Ti and Si into the BST films.[5,6] Nevertheless, Ti was reported to diffuse through the Pt/TiN layer into the BST film to form TiO_x and oxygen vacancies, when the substrate temperature exceeds 450°C.[6-9] Hence, a TiO_x series capacitor (C_s) with a smaller ε_r, formed at the interface between the BST and the bottom electrode, degrades the total capacitance of the storage node. However, the oxidation of diffused Ti or Si produces oxygen vacancies in the BST films, increasing the leakage current.[6,10] Given the above important concerns, low temperature techniques for BST film growth are necessary to suppress the degradation of total ε_r and the leakage current, during integrated circuit (IC) processing.

In general, a dual-gun radio frequency (rf) sputtering system can reduce the reaction energy better than single-gun rf sputtering system can, theoretically. The $BaTiO_3$ and $SrTiO_3$, mixed in the same sputtering target for the single-gun sputtering, have different activation energies, so it is more difficult to control the film qualities by sputtering the single target with two phases than it is by sputtering the two individual targets with single phase. In this work, (Ba, Sr)TiO_3 films were deposited by dual-gun rf sputtering on a Pt/TiN/Ti/Si substrate using two individual targets, $BaTiO_3$ and $SrTiO_3$, simultaneously. Although a low temperature technique is required for the deposition of BST in the integrated circuit (IC) process, controlling the crystallinity and dielectric constant is normally more difficult with a low temperature technique than with a high temperature technique. Controlling the gas mixing ratio during the sputtering of BST is a critical quality issue since the substrate temperature remains under 450°C. Oxygen vacancies are generated in BST films sputtered in Ar ambient, because of oxygen degassing.[7,11] The presence of oxygen vacancies degrades the electrical properties of BST films, so O_2 gas is introduced in the sputtering of BST to compensate these oxygen vacancies.

The effects of the $O_2/Ar + O_2$ ratio (OMR) for the BST/Pt/oxide films have been reported by Tsai *et al.*, but very few works have reported the effects of OMR for the BST films deposited onto the Pt/TiN/Ti/Si substrate using the dual-gun rf sputtering system.[7-9,11] The effects of the OMR on the structures and on the dielectric behaviors of BST films using low temperature depositions are investigated. Optical emission spectroscopy was employed to examine the deposition rate of BST films at various OMRs. A multilayer structure of Pt/BST/Pt/TiN/Ti/Si was employed to study correlations among the electrical properties and OMR; the corresponding mechanisms are discussed.

Experimental

Multilayer specimen of Pt/BST/Pt/TiN/Ti/Si was employed to simulate the practical COB structure of the DRAM capacitor. The starting p-type Si(100) wafers were cleaned by the standard RCA cleaning process. The stacked TiN/Ti layers with 150/50 nm thickness were sputtered onto the Si substrates and rapid thermal annealing (RTA) treated in N_2 ambient at 600°C for 90 s. TiN/Ti layers, densified by RTA, can effectively prohibit the interdiffusion of Ti and Si during the BST thermal process, as reported in our previous works.[6,12,13] The bottom electrodes, 150 nm thick Pt films, were dc sputtered at room temperature.

There are many controversial arguments about the definition of ''substrate temperature.'' In general, the thermal couple sensor (TCS) is embedded between the stainless steel holder and wafer back side to prevent the TCS from the plasma damage and disturbance, particularly for the commercial rf-sputtering system. Thus, the substrate temperature of rf-sputtering system in many reports is measured at the interface between the stainless steel holder/wafer back side,[7-9] and this temperature is much lower than that measured

* Electrochemical Society Active Member.
z E-mail: bschiou@cc.nctu.edu.tw

at wafer's upper surface. Hence, the substrate temperature (300°C), denoted in this paper, was calibrated at the upper surface of the wafer, and the temperature at the wafer back side is about 410°C. BST films (100 nm) were deposited onto Pt/TiN/Ti/Si at 300°C. The chamber pressure was kept at 7 mTorr, and the OMR was regulated by gas flow rate. In general, the chamber gas ambient has a lowest fluctuation of the gas mixing uniformity and the flow rate control during rf sputtering. Thus, the larger scales of OMR conditions are chosen as 0, 5, 12.5, 25, and 50% in this study to prevent the disturbance of ambient fluctuations during BST film sputtering. $BaTiO_3$ (BTO) and $SrTiO_3$ (STO) targets were used simultaneously. Besides, BTO and STO targets are applied individually to check the deposition rate of BTO and STO thin films. The Ba/Sr ratio can be controlled by tuning the rf powers applied to the targets, and, in this study, the sputtering powers were fixed at 175 and 230 W for BTO and STO targets, respectively. Pt top electrodes were deposited on BST films by dc sputtering with 150 μm diam of the top electrode area defined by the shadow mask.

The thickness of BST film was checked by both n & k analyzer (n & k analyzer 1200, n & k Technology Inc.) and field emission scanning electron microscopy (FESEM), (S-4000, Hitachi Co.). Optical emission spectra of plasma near BTO and STO targets were obtained using a 500 mm monochromator (SpectroPro-500, ARC Co.) equipped with 1200 g/mm grating. These spectra could verify that the chemical and physical adsorption happened on target surface. An X-ray diffractometer (D5000, Siemens Co.) was employed to analyze the film structure and grain size, and the compositions of BST films were inspected by both Rutherford backscattering spectrometer (RBS) and peak shift of X-ray diffraction (XRD) patterns. In addition, the BST films are sputtered onto the SiO_2/Si substrates for the RBS measurements in this study, and the Sr/Ba ratio is reasonably the same as that of the BST prepared on the Pt substrate under the same deposition conditions: ambient gas, sputtering powers, and substrate temperature. The Auger electron spectroscopy (AES) was also conducted to study the penetration of oxygen atoms at the Pt/TiN/Ti layers during BST sputtering. Besides, the grain size was doubly checked by FESEM and transmission electron microscopy (TEM). Atomic force microscope (AFM, DI Nano-Scope III, Digital Instruments Co.) was used to inspect the surface morphology. The capacitance and tangent loss were measured by an impedance/gain-phase analyzer (HP 4194A, Hewlett Packard Co.) and double checked with a capacitance-voltage (C-V) analyzer (Package 82 system C-V 590, Keithley Co.). An automatic measurement system that combines an IBM PC/AT, a semiconductor parameter analyzer (HP4156, Hewlett Packard Co.), and a probe station was used to measure the leakage current and lifetime.

Results and Discussion

Figure 1 shows a cross-sectional FESEM micrograph of the BST/Pt/TiN/Ti/Si capacitor, with the BST film deposited at 300°C. Figure 2a reveals that the deposition rate of BST films drops dramatically when oxygen is introduced into the sputtering ambient. Figure 2b indicates that the individual deposition rates of STO and BTO, show the same tendency as Fig. 2a. The optical emission spectra of both Ar and Sr plasma near the STO target were therefore analyzed during sputtering in pure Ar (0% OMR) and 2.5% OMR ambient, as shown in Fig. 3. The intensity decay of Sr plasma (λ = 460.7 nm, from 0 to 2.5% OMR ambient) is much more prominent (as shown in Fig. 3a, b) than that of Ar plasma (λ = 763.5 nm, from 0 to 2.5% OMR ambient, as shown in Fig. 3c, d). That is, the generation of Sr plasma is suppressed in the presence of oxygen. The spectra of the STO target sputtered in even higher OMR show similar results. These spectra imply that sputtering $SrTiO_3$ molecules with Ar^+ ions in O_2/Ar mixed ambient is difficult. The oxygen ions are reported to induce reactive sputtering and form oxide on the target surface, and the presence of oxide decreases the sputtering rate due to the increase in binding energy of the target surface.[14-16] Ba/Sr ratios of BST films prepared on

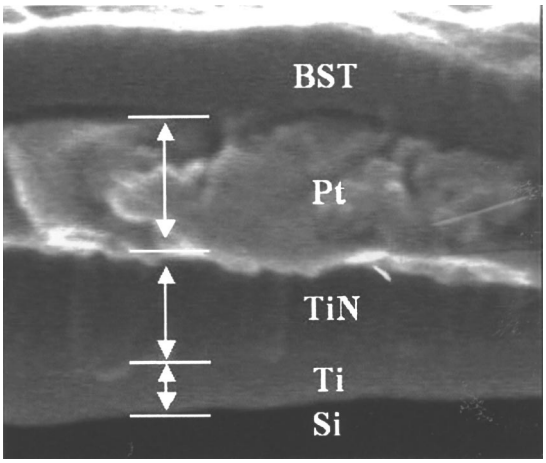

Figure 1. Cross-sectional micrograph of BST/Pt/TiN/Ti/Si capacitor.

SiO_2/Si substrates were obtained by RBS, as shown in Fig. 4. The chemical composition of BST films sputtered in pure Ar ambient are Sr rich, and the Ba/Sr ratio is around 0.38/0.62. As indicated in Fig. 2b, the deposition rate of STO drops faster than that of BTO when oxygen is applied during sputtering. The Ba/Sr ratio thus increases in the O_2/Ar mixed ambient and remains almost constant at 0.5/0.5 at a higher OMR (≧5%) for fixed sputtering powers, as shown in Fig. 4. The dielectric constant of powder BST generally increases with Ba/Sr ratio, but that of thin BST films must be considered with several other factors, as discussed later.

Figure 5 gives XRD patterns of BST films deposited at various OMR. Among the conditions studied, BST film deposited in 12.5% OMR exhibits a best crystallinity. Figure 6a and b indicates that the AES spectra of the BST films sputtered in 5 and 25% OMR, respectively. No oxygen atoms penetrate into the TiN/Ti layers under 5% OMR, as shown in Fig. 6a, but, intriguingly, the oxygen atoms penetrate into the TiN/Ti layers at 25% OMR, as shown in Fig. 6b. According to Fig. 5, the XRD intensity of TiN(111) is strongly enhanced at 5% OMR, but that degrades above 12.5% OMR. The deposition rate of the BST films sputtered in 5% OMR is much lower than that in 0% OMR, so the longer thermal cycling time will enhance the crystallinity of TiN/Ti layers. On the other hand, Fig. 6b indicates the oxygen atoms penetrate the Pt film into TiN/Ti layers above 12.5% OMR, and thus the TiN/Ti layers react with the oxygen atoms, degrading this substrate. The crystallinity of the BST film is strongly affected by the qualities of Pt/TiN/Ti substrate, as reported in previous works.[6,12,13] Hence, the crystallinity of the BST films degrades above 12.5% OMR due to the TiN/Ti substrate damaged by the penetrating oxygen atoms.

The grain size of BST films is estimated from the full width at half-maximum (fwhm) of the XRD patterns, using the Scherrer formula (grain size <100 nm)

$$D_{cal} = 0.89\lambda/(B \times \cos\theta) \quad [1]$$

where D_{cal} is the mean calculated grain size; λ is the X-ray wavelength (~0.154 nm); B is the fwhm of the XRD peak, and θ is the diffraction angle.[17] The fwhm of the (110) peak increases with OMR, and the calculated grain sizes are deduced by Eq. 1. Besides, an estimation of grain size from the fwhm is distorted by interfacial stress, so the calculated grain size should be modified by a factor obtained from a reference sample using FESEM imaging. The real grain size is around 8.3 nm at 5% OMR, as reported in previous work.[18] Thus, the calculated grain size should be multiplied by a factor of 1.22 to estimate the real grain sizes under the same substrate conditions.

In this study, relative grain sizes are much more important than absolute grain sizes. The small grain sizes of BST films decrease

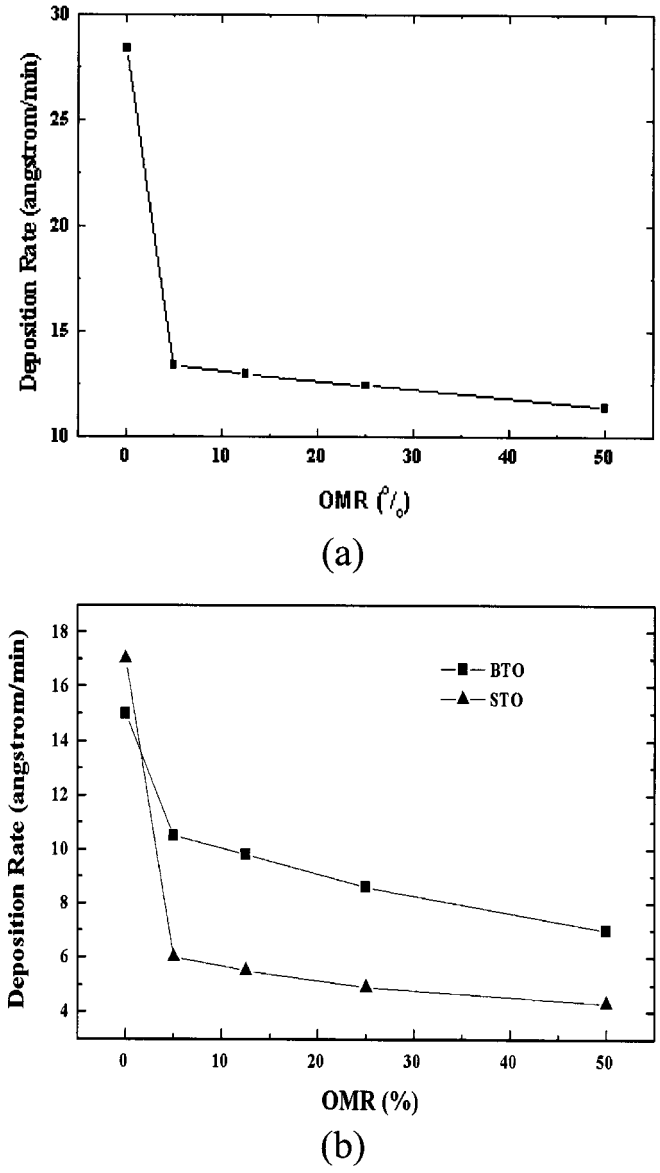

Figure 2. Deposition rate of (a) BST films, (b) individual STO and BTO films *vs.* OMR with sputtering power 230/175 W applied on STO/BTO targets, respectively.

from 15 to 7 nm as OMR increases from 0 to 50%, as depicted in Fig. 7a, suggesting that films prepared at a higher OMR have a smaller grain size; other work has revealed a similar trend.[7,11,19] Besides, Fig. 7a indicates that the strongest peaks of BST(100) and (110) textures are obtained for the samples sputtered at 12.5% OMR. Moreover, Fig. 7b shows that the dielectric constant increases with OMR, reaching a maximum of 364 at 5% OMR, and then decreasing as OMR increases further. Figure 7a shows that best crystallinity occurs at 12.5% OMR and the grain size of the film shrinks as OMR increases. Many factors influence the dielectric constant of BST films such as composition, crystallinity, grain size, and interface quality. A high Ba/Sr ratio and good crystallinity enhances the polarization of electric dipoles in a single grain,[1,7,20] but a small grain size tends to depress the dielectric constant, as reported in previous work.[7,11,21] Hence, the dielectric constant is inferred to increase as the crystallinity improves and as Ba/Sr ratio increases; but over 5% OMR the grain size effect dominates and the dielectric constant decreases as OMR further increases.

Figures 8a and b present the AFM micrographs of BST surface morphology: the films deposited at a higher OMR have smoother

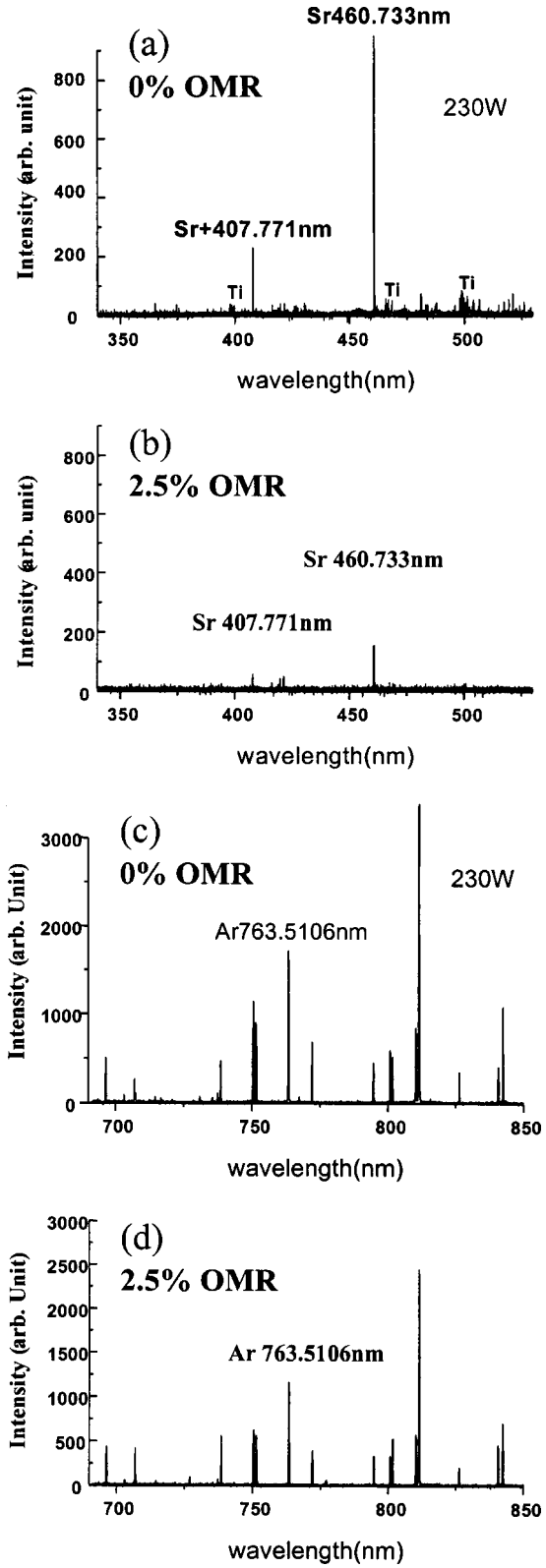

Figure 3. The plasma spectra of (a) Sr plasma in pure Ar ambient, (b) Sr plasma in 2.5% OMR, (c) Ar plasma in pure Ar ambient, and (d) Ar plasma in 2.5% OMR, all detected near $SrTiO_3$ target.

surface. According to Fig. 8a and b, the root mean square (rms) roughness (R_{RMS}) for films deposited in pure Ar ambient is 5.06 nm, while that for films prepared at 12.5% OMR is 2.46 nm. Smaller grain and a lower film deposition rate at higher OMR may result in a smoother surface.

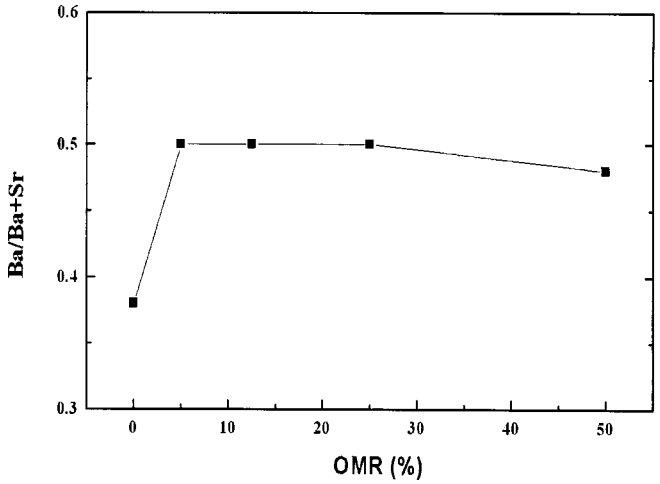

Figure 4. The Ba/Ba + Sr ratio of BST films prepared in various OMR.

Figure 9a indicates the leakage current density decreases as OMR increase. The leakage current of Pt/BST/Pt capacitors may be affected by three factors, namely, the oxygen stoichiometry in the BST films, surface morphology, and the grain boundary. First, the oxygen stoichiometries are different for the BST films prepared in various OMR ambient, according to the following reaction

$$O_o \leftrightarrow V_o^{\bullet\bullet} + 2e' + \tfrac{1}{2}O_2 \qquad [2]$$

where O_o, $V_o^{\bullet\bullet}$, and e' represent the oxygen ion on its normal site, the oxygen vacancy and the electron, respectively. More oxygen vacancies yield a larger leakage current, causing a BST film form to act as an n-type semiconductor.[22,23] Second, smoother surface morphology can prevent the lowering of barrier height by interfacial defects and reduce the local concentrated field to suppress the emission current.[24-26] Third, a BST film, with a narrow bandgap of 3.2-4.0 eV, can normally be considered as semi-insulator or semiconductor, so the grain boundary scattering suppresses the current.[27-29] The reduced grain size with higher OMR forms more grain boundaries to decrease the leakage current. Hence, BST films deposited in higher OMR ambient exhibit compensation of oxygen vacancies, smoother interfaces and smaller grains, all of which reflect the decrease of the leakage current. Figure 9b shows the tangent loss of BST films *vs.* OMR. Tangent loss proceeds by two mechanisms: resistive loss and relaxation loss.[8] In resistive loss case, energy is dissipated by mobile charges, and the tangent loss depends on the magnitude of leakage current; in relaxation loss case, energy is dissipated by relaxation of dipoles, and the tangent loss is proportional to the dielectric constant. Comparing Fig. 9a and b reveals that the trend of the tangent loss against OMR is similar to that of leakage current. Hence, the resistive loss dominates the tangent loss. Figure 9c indicates that the time-zero dielectric breakdown (TZDB) of the Pt/BST/Pt capacitor is enhanced by increasing OMR. BST films sputtered in higher OMR exhibit a higher breakdown field because of their smaller grain size and fewer oxygen vacancies.[7,30]

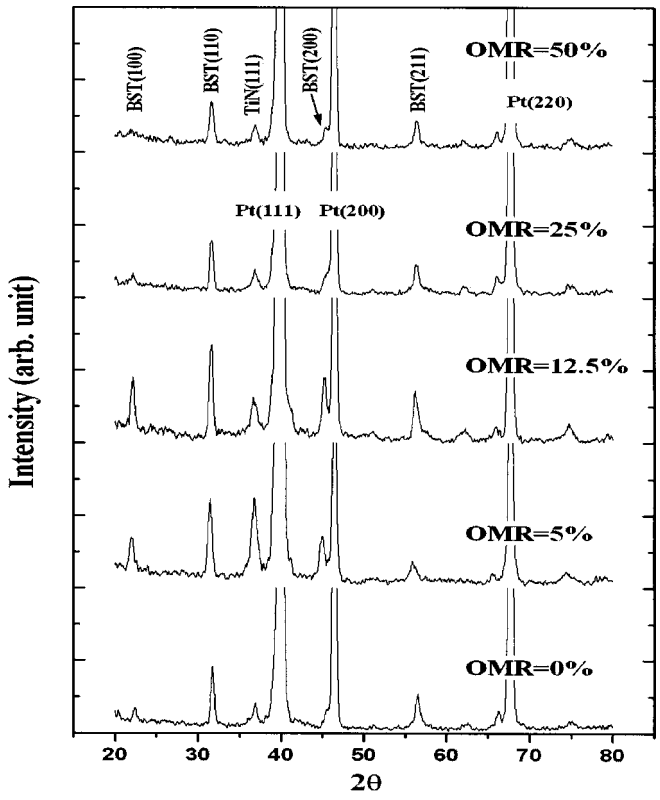

Figure 5. XRD patterns of BST films deposited on Pt/TiN/Ti/Si substrates with various OMR.

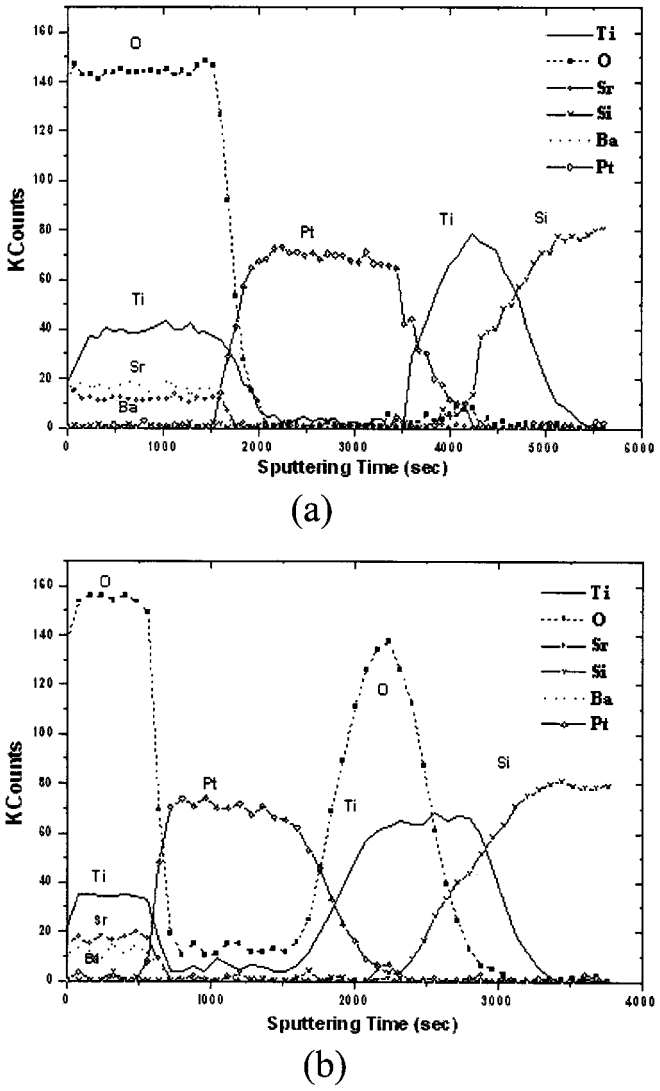

Figure 6. AES spectra of BST films sputtered in (a) 5% and (b) 25% OMR.

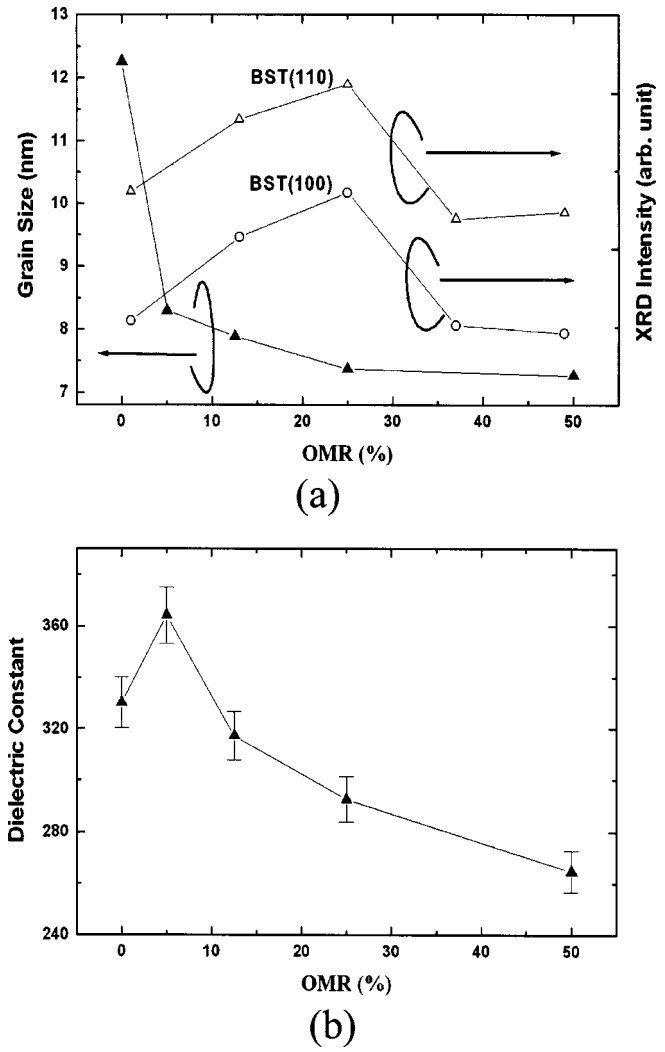

Figure 7. (a) Grain sizes and relative XRD intensities of (100) and (110) textures for the BST films sputtered at various OMR; (b) dielectric constant of BST films prepared at various OMR.

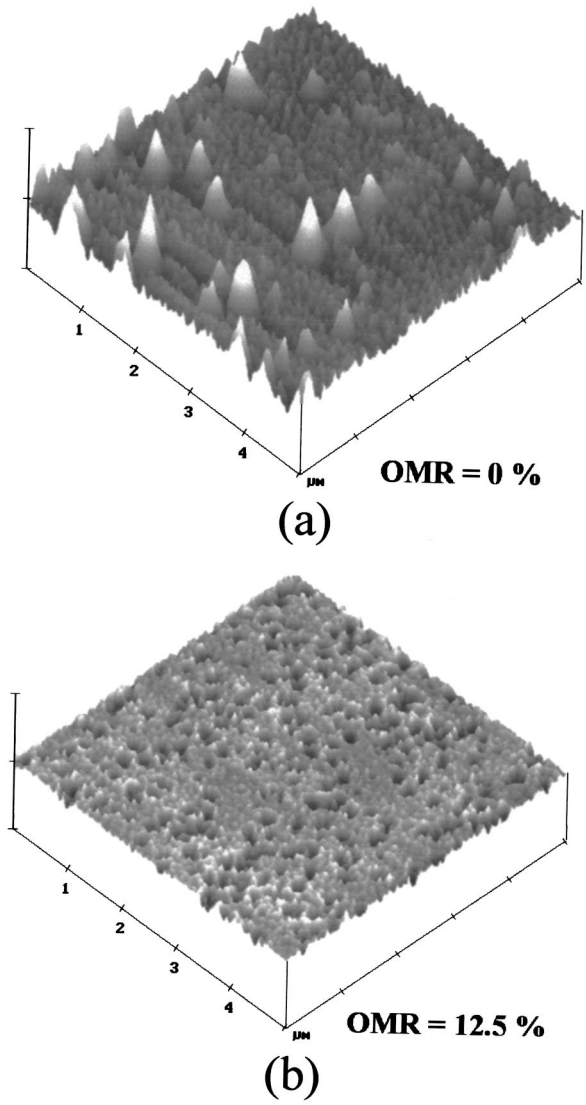

Figure 8. AFM images of BST films deposited in (a) 0% OMR (R_{RMS} = 5.06 nm) and (b) 12.5% OMR (R_{RMS} = 2.46 nm).

The BST films deposited in higher OMR have a longer lifetime, as indicated in Fig. 10. Time-dependent dielectric breakdown (TDDB) is referred to as the resistance degradation of the dielectric ceramic, which slowly increases the leakage current under constant temperature and dc field stress.[6,7,31] The mechanisms of resistance degradations in perovskite films may be generally categorized into the grain boundary model and the reduction model.[31-33] The grain boundary model suggests the presence of very large potential drops across the grain boundaries due to the boundaries' high resistivities. The films with smaller grain sizes form more grain boundaries which the drops in voltage are shared, so the resistance degradation is suppressed. On the other hand, the reduction model suggests that oxygen vacancies and injection electrons cause resistance degradation, which can thus be retarded by a smoother surface and lower oxygen vacancy concentration. Hence, BST films prepared with a higher OMR have a longer lifetime, which result can be attributed to the reduction of the grain sizes, compensation of oxygen vacancies and an improved interface.

Figure 11 gives the C-V relationships of Pt/BST/Pt capacitors with various OMR. The conduction mechanisms of metal/BST/metal capacitors are usually interpreted as Schottky emission (SE, interface-limited conduction) at lower electric fields, and Poole-Frenkel emission (PF, bulk-limited conduction) at higher fields.[9,25,26,34,35] The leakage current governed by SE behavior is expressed as

$$\log(J_{SE}/T^2) = -q[\varphi_{Bu} - (qE/4\pi\varepsilon_d\varepsilon_o)^{1/2}]/(kT \cdot \ln 10) + \log(A^*) \quad [3]$$

where A^* is the effective Richardson's constant; φ_B is the potential barrier height at the surface; ε_d is the dynamic dielectric constant of the ferroelectric material in the infrared region; q is the unit charge; k is Boltzmann's constant; T is temperature, and E is external electric field. The leakage current governed by PF behavior is expressed as

$$\log(J_{PF}/E) = -q[\varphi_t - (qE/\pi\varepsilon_d\varepsilon_o)^{1/2}]/(kT \cdot \ln 10) + \log B \quad [4]$$

where B is a constant and φ_t is the trapped energy level. If the conduction current is governed by PF, then a $\log(J/E)$ against $E^{1/2}$ plot should be a straight line, the slope of which can be used to deduce the dynamic dielectric constant ε_d.[9,25,26,34,35] Similarly, a $\log(J/T^2)$ against $E^{1/2}$ plot can be made for SE. Figure 11a shows the SE plot and Fig. 10b shows the PF plot using the same experimental

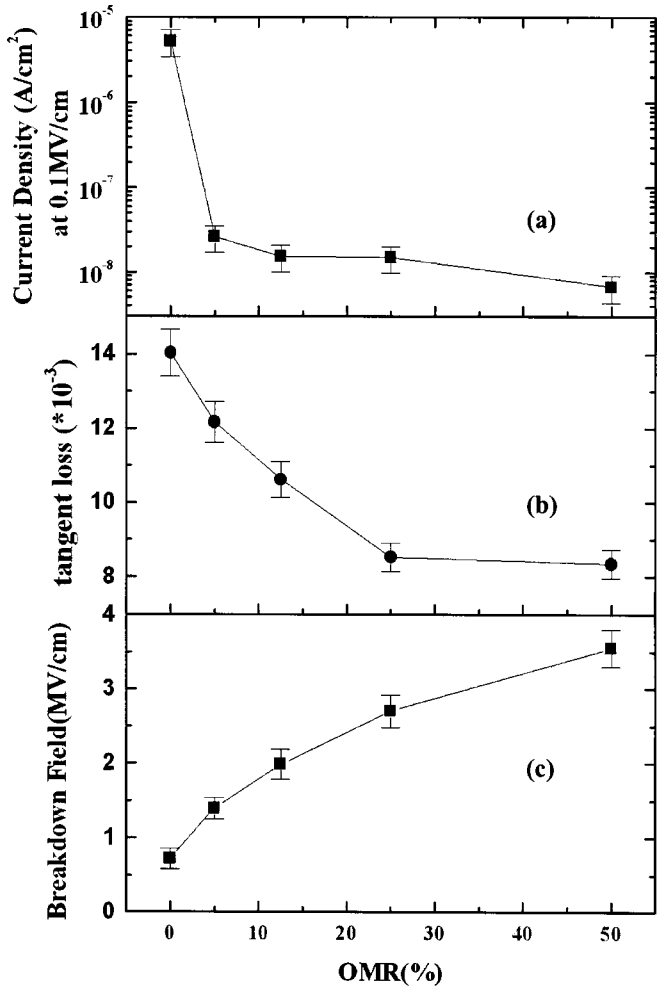

Figure 9. (a) Leakage current density, (b) tangent loss, and (c) the TZDB field of Pt/BST/Pt capacitors prepared in various OMR.

current-voltage (I-V) data in various OMR. The dashed lines are the fitted results. However, the dynamic dielectric constant can be inferred from the optical dielectric constant for an ideal insulating film, and the optical dielectric constant is directly obtained from the square of the refractive index n ($\varepsilon_{opt} = n^2$).[9,26,34,35] Table I lists the

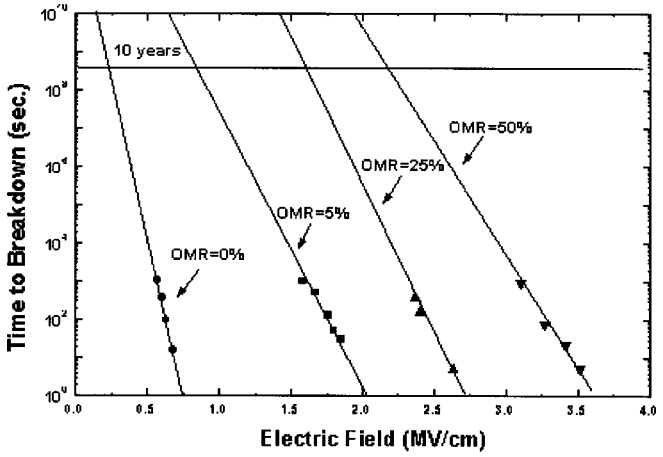

Figure 10. TDDB as a function of electric field of BST films deposited in various OMR.

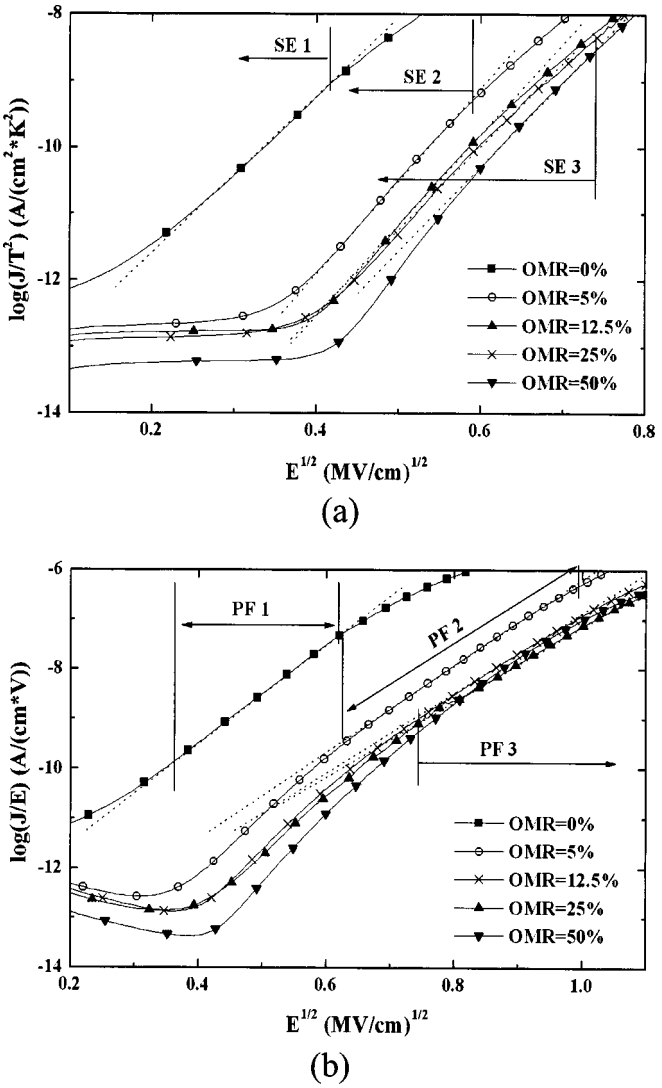

Figure 11. (a) The $\log(J/T^2)$ *vs.* $E^{1/2}$ plot showing SE fitting, and (b) the $\log(J/E)$ *vs.* $E^{1/2}$ plot showing PF fitting for BST films prepared in various OMR.

static, dynamic, and optical dielectric constants of samples prepared at various OMR. In this work, the range of the dynamic dielectric constants (ε_d) calculated by PF fitting is between 2.3 and 4.3, and that calculated by SE fitting is between 1.75 and 2.1. The range of the optical dielectric constant for BST films sputtered with various OMR, measured using an n & k analyzer with λ = 700 nm, is between 3.5 and 5.5. The consistency between dynamic (ε_d) and the

Table I. The dynamic dielectric constant, static dielectric constants, and optical dielectric constants of BST films prepared in various OMR.

OMR (%)	Dynamic dielectric constant		Static dielectric constant	Optical dielectric constant
	PF	SE		
0	2.30	2.09	330	3.53
5	3.19	1.77	364	4.66
12.5	4.18	1.91	317	5.29
25	4.18	2.01	293	4.28
50	4.23	1.98	265	4.34

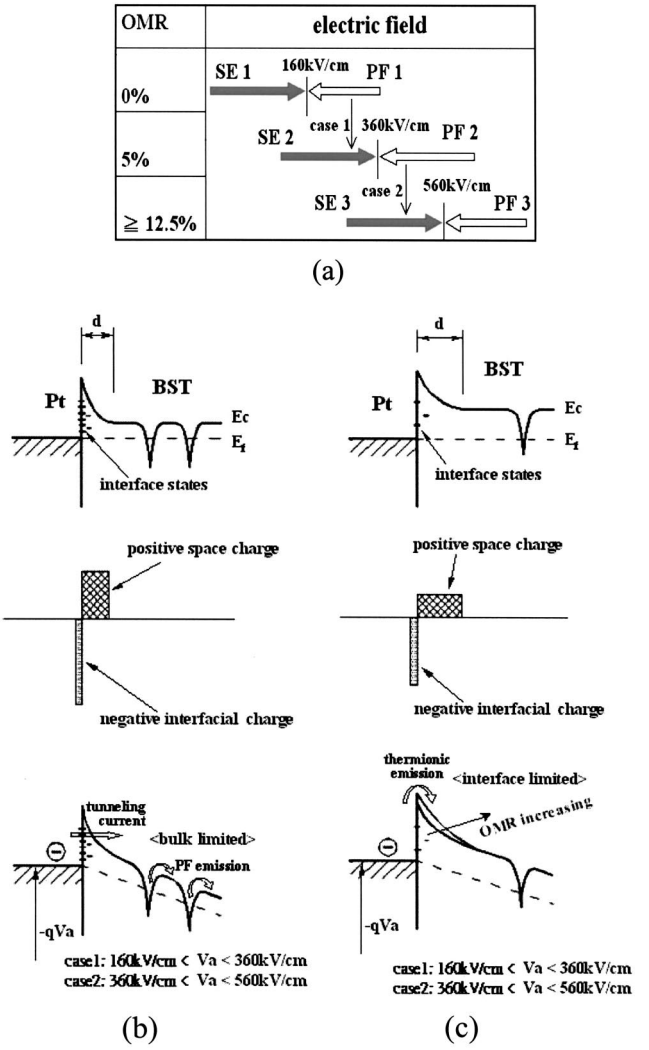

Figure 12. (a) The range of applied field for SE/PF mechanism in various OMR ambient, and the diagrams of the electron energy band in (b) pure Ar or lower OMR ambient and (c) higher OMR ambient.

optical dielectric constant (ε_{opt}) is enough to trust the curve fitting, even though ε_d and ε_{opt} revealed some deviation, perhaps due to the fluctuations of material's density and deformation of its lattice.

Figure 11a and b indicate that Pt/BST/Pt capacitor sputtered at 0% OMR exhibits SE/PF under/above 160 kV/cm, as denoted in the SE 1/PF 1 regions. Figure 11b reveals that $\log(J/T^2)$ curves for 5, 12.5, 25, and 50% OMR are independent of the applied field (E) up to 160 kV/cm, possibly because of the dielectric relaxation of BST films; the curves then increase linearly with $E^{1/2}$ above 160 kV/cm. SE 2 and PF 2 regions show SE/PF behaviors under and above 360 kV/cm in 5% OMR, respectively. SE and PF regions in higher OMR (≧12.5%) are SE 3 and PF 3 regions, respectively.

Figure 12a rearranges the tendencies of the leakage mechanisms, and it reveals that the applied-field boundary of SE/PF linear fitting shifts to a higher field as OMR increases. In case 1, the fitting boundary shifts from 160 kV/cm (SE 1/PF 1) to 360 kV/cm (SE 2/PF 2), as OMR increases from 0 to 5%, and, in case 2, it shifts to 560 kV/cm (SE 3/PF 3), when OMR is equal to or larger than 12.5%. The electron energy bands of the Pt/BST interface are applied to explain the mechanisms of leakage, as presented in Fig. 12b and c. As mentioned above, the BST films can be treated as an n-type semiconductor, and the space charge density of the interfacial depletion region is assumed to be almost equal to the concentration of oxygen vacancies. The relationship between the barrier thickness, d, of the interfacial depletion region and the oxygen vacancy concentration can be derived as

$$d_1/d_2 = \{N_{VO2}/N_{VO1} \times [1 + kT/\Delta \times \ln(N_{VO1}/N_{VO2})]\}^{0.5} \quad [5]$$

where N_{VO} is the concentration of oxygen vacancies; k is Boltzmann's constant; T is temperature, and Δ is the work function difference between Pt and BST. Equation 5 reveals that decreasing the concentration of oxygen vacancies increases the barrier thickness, d, of the interfacial depletion region.[36] Figure 12b indicates that the BST films sputtered in pure Ar or in lower OMR ambient have more oxygen vacancies and a rougher surface than those sputter in higher OMR ambient, yielding a higher interfacial space charge concentration and many interface states to increase the opportunity of tunneling. Furthermore, the magnitude of the leakage current is governed by the balance among the tunneling current, trapping and detrapping rate. Thus, increasing the applied field induces the field-assisted emission of trapped charged carriers (Poole-Frenkel effect), such that the leakage current will be governed by PF emission rate. The bulk-limited mechanism therefore dominates the leakage current at lower OMR and higher applied field. Figure 12c shows that increasing OMR yields fewer interface states, a lower space charge density in the interfacial depletion region and fewer trapping states, by causing a smoother interface and compensating oxygen vacancies. Equation 5 states that a lower space charge density in the interfacial depletion region results in a thicker barrier, and the presence of fewer interface states greatly reduces the opportunity for tunneling. Hence, thermionic emission (SE behavior) is the dominant mechanism of injecting electrons in higher OMR. Consequently, considering cases 1 and 2 of Fig. 12a, the mechanism of the leakage current changes from bulk limited emission (PF) to interface limited emission (SE) as OMR increases.

Conclusions

The deposition rate of low temperature sputtered BST decreases as OMR increases, due to the formation of oxide on the target surface by oxygen ions. Introducing proper oxygen gas during sputtering improves the crystallinity and surface roughness of BST films and changes the Ba/Sr ratio, but decreases the grain size. In addition, the excessive OMR (>12.5%) degrades the crystallinity of BST film due to the TiN/Ti substrate damaged by the penetrations of the oxygen atoms. The dielectric constant is a trade-off determined by compositions, crystallinity and grain size, and the maximum dielectric constant is 364 at 5% OMR. Films prepared at higher OMR have a smaller leakage current density, a lower tangent loss and a longer lifetime, due to compensation of oxygen vacancies, a smother surface morphology and voltage shared by smaller grains.

This study attributed the leakage mechanisms of the Pt/BST/Pt capacitor to (SE)/PF at lower/higher applied field. Part of the PF region changes to SE behavior if OMR increases. In other words, the applied field boundary between SE and PF fittings shifts to a higher field as OMR increases, and this observed I-V behavior is explained by the decrease in the number of interface states and the compensation of oxygen vacancies.

Acknowledgments

This work was supported in part by the Republic of China National Science Council (R.O.C. NSC) under contract NSC 90-2216-E-009-032 and Energy Commission Ministry of Economic Affairs, R.O.C. Thanks are also due to the Semiconductor Research Center (SRC) in National Chiao Tung University and the National Nano Device Laboratory (NDL) of the R.O.C. NSC for their technical support.

National Chiao Tung University assisted in meeting the publication costs of this article.

References

1. T. Kuoiwa, Y. Tsunenine, T. Horikawa, T. Makita, J. Tanimura, N. Mikami, and K. Sato, *Jpn. J. Appl. Phys., Part 1*, **33**, 5187 (1994).
2. A. Qutzourhit, J. U. Trefny, T. Kito, B. Yarar, A. Naziripour, and A. M. Hermann, *Thin Solid Films*, **259**, 218 (1995).
3. S. Onishi, K. Hamada, K. Ishhara, Y. Ito, S. Yokoyama, J. Kudo, and K. Sakiyama, *Tech. Dig. - Int. Electron Devices Meet.*, **1994**, 843.
4. S. R. Summerfelt, *Thin Film Ferroelectric Materials and Devices*, R. Ramesh, Editor, p. 31, Kluwer Academic Publishers, Dordrecht (1997).
5. S. Yamamichi, P.-Y. Lesaicherre, H. Yamaguchi, K. Takemura, S. Sone, H. Yabuta, K. Sato, T. Tamura, K. Nakajima, S. Ohnishi, K. Tokashiki, Y. Hayashi, Y. Kato, Y. Miyasaka, M. Yoshida, and H. Ono, *Tech. Dig. - Int. Electron Devices Meet.*, **1995**, 119.
6. C. C. Hwang, M. H. Juang, M. J. Lai, C. C. Jaing, J. S. Chen, S. Huang, and H. C. Cheng, *Solid-State Electron.*, **45**, 121 (2001).
7. M. S. Tsai, S. C. Sun, and T. Y. Tseng, *J. Appl. Phys.*, **82**, 3482 (1997).
8. M. S. Tsai and T. Y. Tseng, *J. Electrochem. Soc.*, **145**, 2583 (1998).
9. M. S. Tsai and T. Y. Tseng, *J. Electrochem. Soc.*, **145**, 2853 (1998).
10. C. R. Cho, Sook II Kwun, T. W. Noh, and M. S. Jang, *Jpn. J. Appl. Phys., Part 1*, **36**, 2196 (1997).
11. J. Lee, Y. C. Choi, and B. S. Lee, *Jpn. J. Appl. Phys., Part 1*, **36**, 3644 (1997).
12. C. C. Hwang, C. C. Jaing, M. J. Lai, J. S. Chen, S. Huang, M. H. Juang, and H. C. Cheng, *Electrochem. Solid-State Lett.*, **3**, 563 (2000).
13. T. H. Teng, C. C. Hwang, M. J. Lai, S. C. Huang, J. S. Chen, C. C. Jaing, and H. C. Cheng, *Mater. Res. Soc. Symp. Proc.*, **596**, 37 (2000).
14. D. L. Smith D, *Thin-Film Deposition Principles and Practice*, p. 480, McGraw-Hill Inc., New York (1995).
15. S. B. Krupanidhi, H. Hu, and G. R. Fox, *Ferroelectric Thin Films: Synthesis and Basic Properties*, C. Paz de Araujo, J. F. Scott, G. W. Taylor, and S. B. Krupanidhi, Editors, p. 93, Gordon and Breach Publishers, Philadelphia PA (1996).
16. J. Roth, *In Sputtering by Particle Bombardment II*, R. Behrish, Editor, p. 91, Springer-Verlag, New York (1983).
17. B. D. Cullity, *Elements of X-Ray Diffraction*, p. 102, Addison-Wesley Inc., Reading, MA (1978).
18. C. C. Hwang, M. J. Lai, C. C. Jaing, J. S. Chen, S. Huang, M. H. Juang, and H. C. Cheng, *Jpn. J. Appl. Phys., Part 2*, **39**, L1314 (2000).
19. T. Horikawa, N. Mikami, T. Makita, J. Tanimura, M. Kotaoka, K. Sato, and M. Nunoshta, *Jpn. J. Appl. Phys., Part 1*, **32**, 4126 (1993).
20. K. Takemura, S. Yamamichi, P. Y. Lesaicherre, K. Tokashiki, H. Miyamoto, H. Ono, Y. Miyasaka, and M. Yoshida, *Jpn. J. Appl. Phys., Part 1*, **34**, 5224 (1995).
21. K. Okazaki and K. Nagata, *J. Electron. Commun. Soc. Jpn.,*, **C53**, 815 (1970).
22. R. M. Waser, *J. Am. Ceram. Soc.*, **72**, 2234 (1989).
23. D. M. Smyth, M. P. Harmer, and P. J. Peng, *J. Am. Ceram. Soc.*, **72**, 2276 (1989).
24. I. Stolichnov, A. Tagantsev, N. Setter, S. Okhonin, P. Fazan, J. S. Cross, and M. Tsukada, *J. Appl. Phys.*, **87**, 1925 (2000).
25. C. S. Hwang, B. T. Lee, C. S. Kang, J. W. Kim, K. H. Lee, H. J. Cho, H. Horii, W. D. Kim, S. I. Lee, Y. B. Roh, and M. Y. Lee, *J. Appl. Phys.*, **83**, 3703 (1998).
26. C. S. Hwang, B. T. Lee, C. S. Kang, K. H. Lee, H. J. Cho, H. Hideki, W. D. Kim, S. I. Lee, and M. Y. Lee, *J. Appl. Phys.*, **85**, 287 (1999).
27. W. Heywang, *J. Mater. Sci.*, **6**, 1214 (1971).
28. G. T. Mallick, Jr. and P. R. Emtage, *J. Appl. Phys.*, **39**, 3088 (1968).
29. G. E. Pike and C. H. Seager, *J. Appl. Phys.*, **50**, 3414 (1979).
30. L. H. Parker and A. F. Tasch, *IEEE Circuits Devices Mag.*, **1990**, 17 (Jan).
31. M. S. Tsai and T. Y. Tseng, *IEEE Trans. Compon., Packag. Manuf. Technol., Part A*, **23**, 128 (Mar 2000).
32. R. Waser, R. T. Baiatu, and K. H. Hardtl, *J. Am. Ceram. Soc.*, **73**, 1645 (1990).
33. H. Y. Lee and K. L. Lee, *IEEE Trans. Compon., Hybrids, Manuf. Technol.*, **4**, 443 (1984).
34. Y. B. Lin and J. Y. Lee, *J. Appl. Phys.*, **87**, 1841 (2000).
35. R. M. Hill, *Thin Solid Films*, **8**, R21 (1971).
36. M. S. Tyagi, *Metal-Semiconductor Schottky Barrier Junctions and Their Applications*, B. L. Sharma, Editor, p. 27, Plenum Press, New York (1984).